Chem

CellPress
OPEN ACCESS

Article

Breaking the trade-off between selectivity and adsorption capacity for gas separation

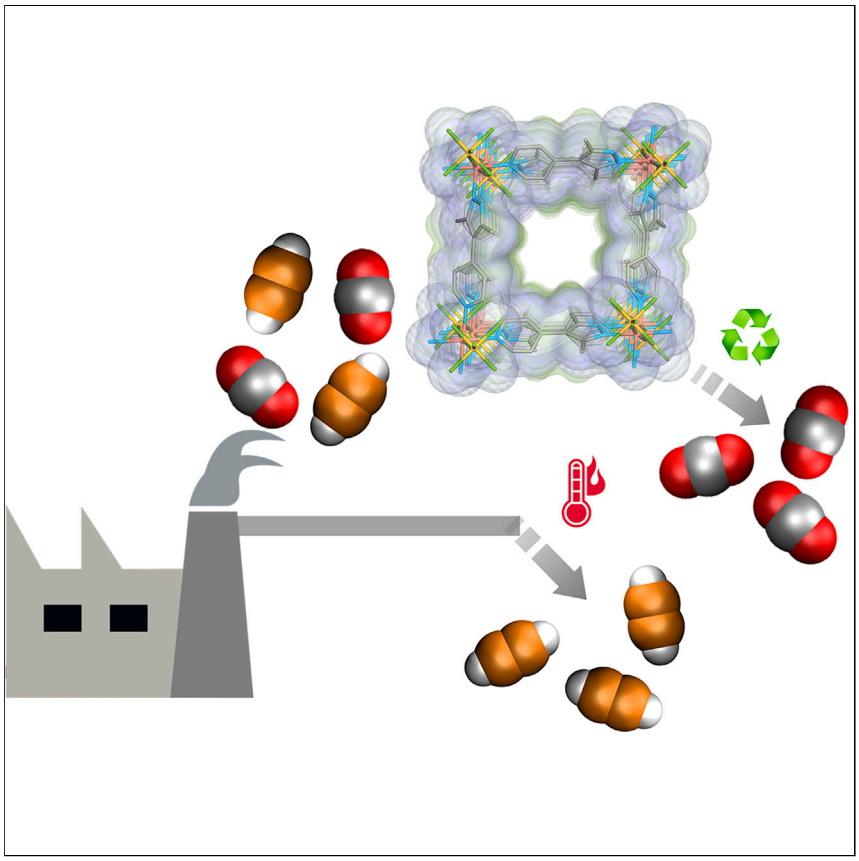

A new family of six isostructural hybrid ultramicroporous materials that enabled high adsorption capacity as well as high experimental separation selectivity values for C_2H_2/CO_2 separation.

Naveen Kumar, Soumya Mukherjee, Nathan C. Harvey-Reid, ..., Yining Huang, Paul E. Kruger, Michael J. Zaworotko

xtal@ul.ie

Highlights

Six isostructural hybrid ultramicroporous materials are prepared and characterized

Crystal engineering approach enabled fine-tuning of pore size and chemistry

Weak CO_2/strong C_2H_2 affinity resulted in high C_2H_2/CO_2 separation selectivities

SIFSIX-21-Ni: benchmark selectivity/uptake capacity for C_2H_2/CO_2 separation

Kumar et al., Chem 7, 3085–3098
November 11, 2021 © 2021 The Authors.
Published by Elsevier Inc.
https://doi.org/10.1016/j.chempr.2021.07.007

Chem

CellPress
OPEN ACCESS

Article

Breaking the trade-off between selectivity and adsorption capacity for gas separation

Naveen Kumar,[1,7] Soumya Mukherjee,[1,7] Nathan C. Harvey-Reid,[2] Andrey A. Bezrukov,[1] Kui Tan,[3] Vinicius Martins,[4] Matthias Vandichel,[1] Tony Pham,[5] Lisa M. van Wyk,[6] Kolade Oyekan,[3] Amrit Kumar,[1] Katherine A. Forrest,[5] Komal M. Patil,[2] Leonard J. Barbour,[6] Brian Space,[5] Yining Huang,[4] Paul E. Kruger,[2] and Michael J. Zaworotko[1,8,*]

SUMMARY

The trade-off between selectivity and adsorption capacity with porous materials is a major roadblock to reducing the energy footprint of gas separation technologies. To address this matter, we report herein a systematic crystal engineering study of C_2H_2 removal from CO_2 in a family of hybrid ultramicroporous materials (HUMs). The HUMs are composed of the same organic linker ligand, 4-(3,5-dimethyl-1*H*-pyrazol-4-yl)pyridine, pypz, three inorganic pillar ligands, and two metal cations, thereby affording six isostructural pcu topology HUMs. All six HUMs exhibited strong binding sites for C_2H_2 and weaker affinity for CO_2. The tuning of pore size and chemistry enabled by crystal engineering resulted in benchmark C_2H_2/CO_2 separation performance. Fixed-bed dynamic column breakthrough experiments for an equimolar (v/v = 1:1) C_2H_2/CO_2 binary gas mixture revealed that one sorbent, SIFSIX-21-Ni, was the first C_2H_2 selective sorbent that combines exceptional separation selectivity (27.7) with high adsorption capacity (4 mmol·g^{-1}).

INTRODUCTION

Acetylene (C_2H_2) is an important chemical commodity; it is used to manufacture vinyl and acrylate polymers and is a combustion fuel in oxy-acetylene torches.[1,2] The latter application stems from its flammability range, the widest known (2.5%–81%), but can thereby represent an explosion hazard at >2.5% concentrations.[3] Whereas the utility of C_2H_2 as an oxy-combustion fuel typically requires >98% purity grade for its use as a chemical feedstock, a higher purity grade is essential.[4] Bulk C_2H_2 is produced by either oxidative coupling (partial combustion) of methane or downstream thermal cracking of hydrocarbons; CO_2 is a by-product of both processes.[5] C_2H_2 production generates CO_2 as an impurity, which means that selective separation/purification of high-purity (>99% v/v) C_2H_2 from C_2H_2/CO_2 mixtures is of industrial relevance.[6] Three technologies are currently used to remove C_2H_2 from C_2H_2/CO_2 mixtures: (1) bulk solvent extraction, resulting in solvent waste such as *N*,*N*-dimethylformamide and acetone[7]; (2) partial hydrogenation of C_2H_2 to ethylene, C_2H_4, with costly noble-metal catalysts such as Ag(0)[8]; and (3) cryogenic distillation, an energy-intensive process.[9] All three processes suffer from high cost and low efficiency. Physisorbents offer potential for energy-efficient gas purification as exemplified by recent reports on physisorbents that exhibit benchmark performance for key separations such as CO_2/N_2,[10,11] CO_2/CH_4,[12] C_2H_2/C_2H_4,[13,14] and C_2H_6/C_2H_4,[15] among others.[16] Nevertheless, commercially viable C_2H_2 capture from CO_2 using physisorbents remains an unmet challenge since traditional physisorbents, such as zeolites, mesoporous silicas, and activated carbons, exhibit poor selectivity

The bigger picture

It is generally recognized that porous solids (sorbents) with high selectivity and high adsorption capacity offer potential for energy-efficient gas separations. Unfortunately, there is generally a trade-off between capacity and selectivity, which represents a roadblock to the utility of sorbents in key industrial processes. For example, acetylene (C_2H_2), an important fuel and chemical intermediate, is produced with CO_2 as an impurity, and the similar physicochemical properties of C_2H_2 and CO_2 mean that most sorbents are poorly selective. Hybrid ultramicroporous materials (HUMs) are candidates for gas separations as they exhibit benchmark selectivity for several key gas pairs. Unfortunately, existing HUMs are handicapped by low capacity. We report a new HUM, SIFSIX-21-Ni, that addresses the trade-off between selectivity and capacity that has plagued sorbents, as its high uptake and high selectivity renders it the new benchmark for C_2H_2/CO_2 separation performance.

for C_2H_2 over CO_2[17] thanks to their similar physicochemical properties (molecular dimensions: C_2H_2 = 3.32 × 3.34 × 5.7 Å^3; CO_2 = 3.18 × 3.33 × 5.36 Å^3; kinetic diameters for both molecules = 3.3 Å; boiling points: C_2H_2 = 189.3 K, CO_2 = 194.7 K).[18,19] These physicochemical properties also practically rule out the application of molecular sieving.[20]

In this context, metal-organic materials (MOMs),[21] also known as metal-organic frameworks (MOFs)[22,23] or porous coordination polymers (PCPs),[24] have emerged as sorbent candidates to serve as C_2H_2 selective physisorbents in C_2H_2/CO_2 separation.[25] Unlike traditional classes of sorbents, the modularity of MOMs enables fine-tuning of pore size and pore chemistry using crystal engineering design approaches.[21] Nevertheless, there are >100,000 MOMs in the CSD MOF subset (2020.3 CSD release).[26] To the best of our knowledge, only a few (20) have been experimentally studied for C_2H_2/CO_2 separation under dynamic conditions (e.g., dynamic column breakthrough [DCB] experiments, see Table S1) including recently reported benchmarks set by **ATC-Cu**,[27] **FJI-H8-Me**,[28] and **SIFSIX-Cu-TPA**.[29] For example, **ATC-Cu** was found to exhibit an ideal adsorbed solution theory (IAST) selectivity of 53.6 for 1:1 C_2H_2/CO_2 separation.[27] The need to study sorbent performances under dynamic conditions arises because calculation of separation performance from C_2H_2 and CO_2 single-component isotherms tends to overestimate separation performance. IAST and fixed-bed simulated breakthrough calculations are, therefore, indicative rather than confirmative. Our review of the literature reveals that C_2H_2/CO_2 separation selectivity (α_{AC}) values for equimolar (v/v) mixtures have been experimentally measured for only 16 sorbents, most of which are classified as MOFs: **SIFSIX-Cu-TPA**,[29] **TCuI**,[30] **TCuBr**,[30] **TCuCl**,[30] **JCM-1**,[31] **NKMOF-1-Ni**,[32] **FJU-22a**,[33] **FJU-89a**,[34] **HOF-3**,[35] **FJU-6-TATB**,[36] **SSNU-45**,[37] **JXNU-5**,[38] **FJU-36a**,[39] **FeNiM′MOF**,[40] **UTSA-74a**,[41] and **sql-16-Cu-NO$_3$-α′**.[42] Whereas these results are promising, they do not fully address the *spectrum of performance parameters* needed before a material can be considered for commercialization.[43] In particular, in addition to selectivity, working capacity and recyclability (including the kinetics and energy of regeneration) are also key performance parameters.[25,44] As revealed in Table S1, **UTSA-74a** is the only sorbent that offers separation selectivity ≥5 and adsorption capacity ≥3.5 mmolg^{-1}. Unfortunately, **UTSA-74a** requires a high temperature for sorbent regeneration and activation (473 K under high vacuum) to generate the unsaturated metal centers (UMCs) that drive preferential binding for C_2H_2 over CO_2.

Hybrid ultramicroporous materials (HUMs), sorbents that exhibit <0.7 nm pore diameter and are comprised of both organic and inorganic linker ligands, are an emerging subclass of MOMs.[45] HUMs are outstanding candidates for physisorptive separation of small gas sorbates as they offer benchmark adsorption selectivities for C_2H_2 over C_2H_4 (S_{AE})[14,18] and CO_2 over N_2 (S_{CN}).[16,19,46] This performance has been attributed to two key features that enhance selective binding: (1) narrow pore sizes and (2) pore surfaces/walls offering strong electrostatics. HUMs are also modular, which enables crystal engineering-driven control of pore size and chemistry to facilitate removal of even trace impurities. Unfortunately, narrow pore size, as seen in the prototypal pyrazine-linked HUMs, tends to limit surface area and uptake capacity. We recently reported that an HUM based on an expanded symmetrical ligand, 3,3′,5,5′-tetramethyl-1*H*,1′*H*-4,4′-bipyrazole, pzpz, offered a highly selective CO_2 binding site that was also hydrophobic.[11] Six members of a new HUM platform based on an unsymmetrical ligand that is related to pzpz, 4-(3,5-dimethyl-1*H*-pyrazol-4-yl)pyridine (pypz) are introduced herein. The six HUMs were obtained by inorganic ligand (SiF_6^{2-}, SIFSIX; TiF_6^{2-}, TIFSIX; and $NbOF_5^{2-}$, NbOFFIVE) and/or metal

[1]Bernal Institute, Department of Chemical Sciences, University of Limerick, Limerick V94 T9PX, Republic of Ireland

[2]MacDiarmid Institute for Advanced Materials and Nanotechnology, School of Physical and Chemical Sciences, University of Canterbury, Private Bag 4800, Christchurch 8140, New Zealand

[3]Department of Materials Science & Engineering, University of Texas at Dallas, Richardson, TX 75080, USA

[4]Department of Chemistry, the University of Western Ontario, 1151 Richmond Street, London, ON N6A 5B7, Canada

[5]Department of Chemistry, University of South Florida, 4202 East Fowler Avenue, CHE205, Tampa, FL 33620-5250, USA

[6]Department of Chemistry and Polymer Science, University of Stellenbosch, Stellenbosch, Matieland 7602, South Africa

[7]These authors contributed equally

[8]Lead contact

*Correspondence: xtal@ul.ie

https://doi.org/10.1016/j.chempr.2021.07.007

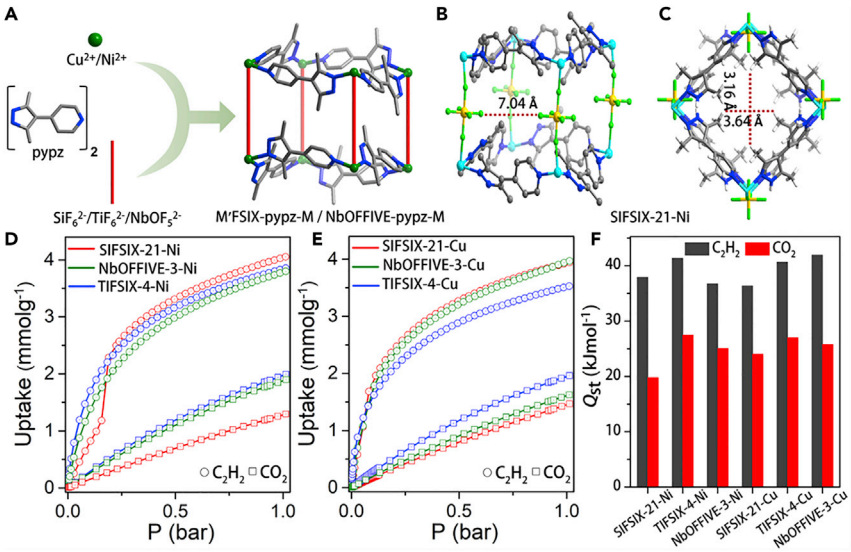

Figure 1. The family of isostructural HUMs reported herein and their single-crystal X-ray structures, single-component adsorption isotherms, and isosteric heats of adsorption

(A) Schematic illustration of the building blocks and pcu network topology of **M′FSIX-pypz-M** and **NbOFFIVE-pypz-M**.

(B) C_2H_2 binding site in **SIFSIX-21-Ni** viewed across diagonally opposite F atoms of SiF_6^{2-} pillars.

(C) The ultramicropore in **SIFSIX-21-Ni** viewed along the crystallographic *b* axis.

(D) C_2H_2 and CO_2 isotherms of **SIFSIX-21-Ni**, **NbOFFIVE-3-Ni**, and **TIFSIX-4-Ni** at 298 K.

(E) C_2H_2 and CO_2 isotherms of **SIFSIX-21-Cu**, **NbOFFIVE-3-Cu**, and **TIFSIX-4-Cu** at 298 K.

(F) Comparative bar diagram of isosteric heat of adsorptions (C_2H_2 and CO_2). (Color codes in Figures 1A–1C: C, gray; N, blue; Si, yellow; F, light green; Ni, cyan.)

(Ni^{2+} or Cu^{2+}) substitution (Figure 1A) and offer higher gravimetric surface areas (and, therefore, potentially higher working capacity) than the corresponding pyrazine-linked HUMs.[47] Herein, we report the exceptional adsorptive separation performance for C_2H_2 versus CO_2 of these HUMs as evaluated by single-component gas sorption measurements, dynamic gas breakthrough experiments, *in situ* IR studies, solid-state NMR experiments, and molecular modeling.

RESULTS AND DISCUSSION

Synthesis and structural characterization

Single crystals of **SIFSIX-21-Ni**, **TIFSIX-4-Ni**, **SIFSIX-21-Cu**, and **TIFSIX-4-Cu**, and microcrystalline samples of **NbOFFIVE-3-Ni** and **NbOFFIVE-3-Cu** were prepared as detailed in the supplemental information. Single-crystal X-ray diffraction (SCXRD) studies revealed that **SIFSIX-21-Ni**, **TIFSIX-4-Ni**, **SIFSIX-21-Cu**, and **TIFSIX-4-Cu** are isostructural and crystallize as **pcu** topology networks in orthorhombic space group *Pnna*. The crystallographic data and refinement parameters for **SIFSIX-21-Ni**, **TIFSIX-4-Ni**, **SIFSIX-21-Cu**, and **TIFSIX-4-Cu** are presented in Table S2. The unit cell parameters calculated from powder X-ray diffraction (PXRD) for **NbOFFIVE-3-Cu** and **NbOFFIVE-3-Ni** are close to those of the M′FSIX analogs (Figures S3 and S4). Unit cell volumes are as follows: **TIFSIX-4-Cu** (3,458.8 $Å^3$)> **SIFSIX-21-Cu** (3,361.1 $Å^3$)> **NbOFFIVE-3-Cu** (3,338 $Å^3$)> **TIFSIX-4-Ni** (3,291.7 $Å^3$)> **NbOFFIVE-3-Ni** (3,236 $Å^3$)> **SIFSIX-21-Ni** (3,199.2 $Å^3$). Solvent-accessible free volumes were calculated to be *ca.* 30%. Polycrystalline samples of **SIFSIX-21-Ni**, **TIFSIX-4-Ni**, **SIFSIX-21-Cu**, and **TIFSIX-4-Cu** used for physicochemical characterization and sorption studies were prepared solvothermally in methanol (see supplemental information for details). Bulk phase purity was established by comparison of experimental and calculated PXRD patterns (Figures S1 and S2). Thermogravimetric

analysis and variable temperature PXRD (VT-PXRD) experiments revealed each material retained crystallinity as follows: 613 K (**NbOFFIVE-3-Ni**) > 573 K (**TIFSIX-4-Ni**) > 513 K (**SIFSIX-21-Ni**); 533 K (**TIFSIX-4-Cu**) > 513 K (**NbOFFIVE-3-Cu**) > 493 K (**SIFSIX-21-Cu**) (Figures S5–S10 and S13–S14).

Single-component gas isotherms and binding sites

To evaluate microporosity, N_2 and CO_2 adsorption isotherms were measured at 77 K and 195 K, respectively (Figures S15, S17, S19, S21, S23, and S25). Following the Rouquerol criteria,[48] Brunauer-Emmett-Teller (BET) surface areas were experimentally determined from the N_2 adsorption isotherms as follows: **TIFSIX-4-Ni** (931 m^2g^{-1}) > **SIFSIX-21-Ni** (871 m^2g^{-1}) > **SIFSIX-21-Cu** (839 m^2g^{-1}) > **NbOFFIVE-3-Cu** (805 m^2g^{-1}) > **NbOFFIVE-3-Ni** (761 m^2g^{-1}) > **TIFSIX-4-Cu** (747 m^2g^{-1}). C_2H_2 and CO_2 single-component gas sorption isotherms were collected at 298 K and 273 K (Figures S16, S18, S20, S22, S24, and S26). All six HUMs were observed to exhibit higher affinity for C_2H_2 than CO_2 with C_2H_2 uptakes >3.5 $mmolg^{-1}$ and CO_2 uptakes <2.0 $mmolg^{-1}$ at 298 K and 1 bar (Figures 1D and 1E). **SIFSIX-21-Ni** was found to exhibit the highest C_2H_2 uptake (~4.05 $mmolg^{-1}$), followed by **NbOFFIVE-3-Cu** (3.97 $mmolg^{-1}$), **SIFSIX-21-Cu** (3.94 $mmolg^{-1}$), **TIFSIX-4-Ni** (3.85 $mmolg^{-1}$), **NbOFFIVE-3-Ni** (3.79 $mmolg^{-1}$), and **TIFSIX-4-Cu** (3.53 $mmolg^{-1}$) (Figures 1D and 1E). The stepped isotherms observed for **SIFSIX-21-Ni** (Figure S16) and **SIFSIX-21-Cu** (Figure S22) prompted us to conduct *in situ* PXRD measurements on these two HUMs. These measurements (Figures S11 and S12) reveal no significant change in the PXRD patterns with C_2H_2 loading until 1 bar indicated that only subtle structural changes occurred during C_2H_2 sorption. Isosteric heats of adsorption, Q_{st}, were determined from virial fits of these experimental single-component gas isotherms. Q_{st} values for CO_2 at zero loading, $Q_{st}(CO_2)$, were as follows: 19.8 kJ mol^{-1} (**SIFSIX-21-Ni**) < 24.0 kJ mol^{-1} (**SIFSIX-21-Cu**) < 25.1 kJ mol^{-1} (**NbOFFIVE-3-Ni**) < 25.8 kJ mol^{-1} (**NbOFFIVE-3-Cu**) < 27.0 kJ mol^{-1} (**TIFSIX-4-Cu**) < 27.5 kJ mol^{-1} (**TIFSIX-4-Ni**). Q_{st} (C_2H_2) values were determined to be as follows: 36.3 kJ mol^{-1} (**SIFSIX-21-Cu**) < 36.7 kJ mol^{-1} (**NbOFFIVE-3-Ni**) < 37.9 kJ mol^{-1} (**SIFSIX-21-Ni**) < 40.6 kJ mol^{-1} (**TIFSIX-4-Cu**) < 41.3 kJ mol^{-1} (**TIFSIX-4-Ni**) < 41.9 kJ mol^{-1} (**NbOFFIVE-3-Cu**) (Figures 1F amd S27–S32; all virial fitting parameters are provided in Figures S33–S44). The differences between $Q_{st}(C_2H_2)$ and $Q_{st}(CO_2)$, $(\Delta Q_{st})_{AC} = [Q_{st}(C_2H_2) - Q_{st}(CO_2)]$, were as follows: 18.1 kJ mol^{-1} (**SIFSIX-21-Ni**) > 16.1 kJ mol^{-1} (**NbOFFIVE-3-Cu**) > 13.9 kJ mol^{-1} (**TIFSIX-4-Ni**) > 13.6 kJ mol^{-1} (**TIFSIX-4-Cu**) > 12.3 kJ mol^{-1} (**SIFSIX-21-Cu**) > 11.6 kJ mol^{-1} (**NbOFFIVE-3-Ni**). These Q_{st} and ΔQ_{st} values reveal the relative thermodynamic preferences of the studied sorbents toward the competing sorbates, C_2H_2 and CO_2. Adsorption selectivities were calculated using IAST.[49] For C_2H_2/CO_2 (v/v: 1:1 and 2:1) at 1 bar and 298 K, IAST selectivities (S_{AC}) were calculated upon fitting the single-component isotherms to the dual-site Langmuir-Freundlich equation (see supplemental information for details; Figures S51, S52, and Table S3). S_{AC} (1:1/2:1) values at 1 bar were thereby determined to be 10.0/9.4 (**SIFSIX-21-Cu**) > 9.5/9.0 (**NbOFFIVE-3-Cu**) > 8.3/8.1 (**TIFSIX-4-Cu**) > 7.8/7.8 (**SIFSIX-21-Ni**) > 7.6/7.4 (**TIFSIX-4-Ni**) > 6.0/5.9 (**NbOFFIVE-3-Ni**) (Figures S45–S50). As presented in Table S1, under relevant partial pressures, S_{AC} for the six HUMs studied in this contribution were found to be comparable to leading C_2H_2-capture sorbents such as **SIFSIX-Cu-TPA**(5.3),[29] **MUF-17**(6),[50] **ZJU-60a**(6.7),[51] **FJU-22a**(7.1),[33] **TCuBr** (9.5),[30] **ZJUT-2a**(10),[52] **TIFSIX-2-Cu-i**(10),[53] **FJI-H8-Me**(10.4),[28] and **MIL-100(Fe)**(12.5).[54]

The binding sites for CO_2 and C_2H_2 in **SIFSIX-21-Ni** were determined by simulated annealing calculations (Figure 2). The binding energies at 0.1 bar obtained from canonical Monte Carlo (CMC) were in agreement with the experimentally derived low loading $Q_{st}(C_2H_2)$ and $Q_{st}(CO_2)$ obtained from single-component isotherms (Table S4). Results derived by these two simulation methods revealed that C_2H_2 molecules

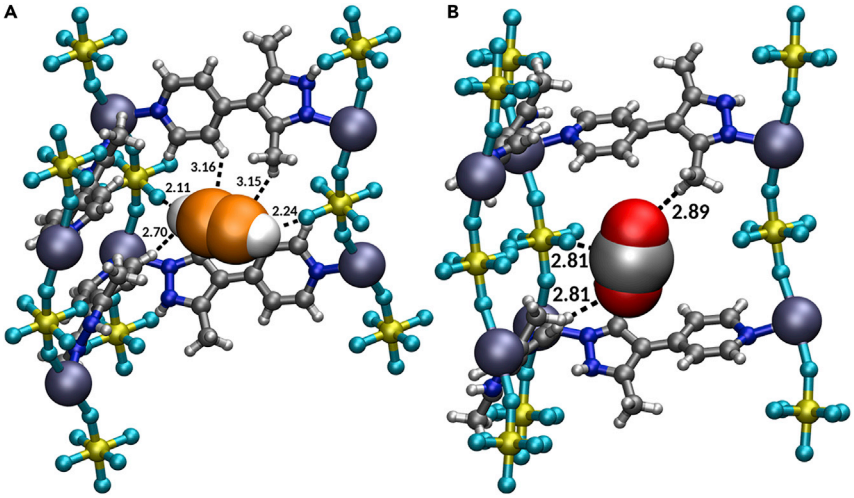

Figure 2. The binding sites in SIFSIX-21-Ni that result in strong C_2H_2 affinity versus CO_2

(A and B) Views of (A) C_2H_2 binding sites and (B) CO_2 binding sites in **SIFSIX-21-Ni** as determined from molecular simulations (C_2H_2 and CO_2 molecules are shown in space-filling model whereas **SIFSIX-21-Ni** is presented in ball-and-stick model) (color codes: N, blue; Si, yellow; F, turquoise; Ni, lilac; O, red; H, white; C, gray, except in the C_2H_2 molecule: orange).

interact with a pair of diagonally opposite F atoms of the inorganic pillars (SiF_6^{2-}) via two $(C_2H_2)CH^{\delta+}\cdots F^{\delta-}$ interactions. There are also $CH\cdots C(C_2H_2)$ interactions. CO_2 molecules form $C^{\delta+}\cdots F^{\delta-}$ and $CH\cdots O(CO_2)$ interactions. To further understand these binding sites, density function theory (DFT) refinements were conducted on the strongest binding sites of **SIFSIX-21-Ni** as identified by CMC simulations in order to calculate the adsorption enthalpies at low loading (one adsorbate molecule per unit cell). Employing the BEEF-vdW functional,[55] adsorption enthalpies of −45.3 and −30.1 kJ mol^{-1} were calculated for C_2H_2 and CO_2, respectively. The adsorption enthalpy difference of 15 kJ mol^{-1} correlates well with experimental ΔQ_{st} values (Figure 1F). For the BEEF-vdW optimized structures (see supplemental information), the optimized binding pocket with adsorbed C_2H_2 has two short $F^{\delta-}\cdots H^{\delta+}$ interactions (2.15 Å each, Figure S53A). For CO_2, $F^{\delta-}\cdots C^{\delta+}$ interactions of 3.69 Å and $CH\cdots O(CO_2)$ interactions of 2.95 and 3.34 Å (Figure S53B) were determined. For CO_2 adsorption, an alternate binding site with similar adsorption enthalpies ($\pm$ 1 kJ mol^{-1}) with shorter $F^{\delta-}\cdots C^{\delta+}$ interactions of 3.10 Å and $CH\cdots O(CO_2)$ interactions of 2.59 and 3.15 Å were observed (Figure S53C). Because the adsorbates maximized their interactions within the binding pocket (Figure S53), these enthalpies are higher than the $Q_{st}(C_2H_2)$ and $Q_{st}(CO_2)$ determined from CMC simulations, the latter representing the average binding energy distribution at a certain pressure. Therefore, the loss in translational entropy was found to be higher for C_2H_2 than for CO_2. Experimental Q_{st} values representing a distribution averaged energy over all possible adsorption configurations of 16.1 kJmol^{-1} (CO_2) and 40.6 kJmol^{-1} (C_2H_2) were found to be slightly lower than the adsorption enthalpies computationally predicted from the optimal binding sites. Therefore, one can conclude that the average residence time of C_2H_2 in its most stable binding site compared with that of CO_2 is higher, suggesting that CO_2 will exhibit faster kinetics. When the CO_2 binding site of **SIFSIX-21-Ni** is compared with that of **SIFSIX-3-Ni**, unlike the single $C^{\delta+}\cdots F^{\delta-}$ binding interaction in **SIFSIX-21-Ni**, **SIFSIX-3-Ni** was found to exhibit four $C^{\delta+}\cdots F^{\delta-}$ binding interactions to electronegative F atoms from four independent SiF_6^{2-} anions.[56] Like **SIFSIX-18-Ni-β**, **SIFSIX-21-Ni** exhibits $C^{\delta+}\cdots F^{\delta-}$ and $CH\cdots O$ interactions with CO_2, however **SIFSIX-18-Ni-β** was found to exhibit multiple $CH\cdots O$ interactions

thanks to the presence of extra methyl groups in pzpz over pypz.[11] Therefore, both **SIFSIX-3-Ni** and **SIFSIX-18-Ni-β** exhibit significantly higher CO_2 binding energies compared with **SIFSIX-21-Ni**.[11,56] Conversely, **SIFSIX-21-Ni** exhibits $CH^{\delta+}\cdots F^{\delta-}$ interactions with C_2H_2 similar to those observed in **SIFSIX-2-Cu-i** and **TIFSIX-2-Cu-i** thanks to their "sweet spots" for C_2H_2 binding (F•••F distance of *ca.* 7 Å, see Figure 1B).[13,53] In summary, the binding sites in the pypz HUMs reported herein combine key features that imply strong C_2H_2 affinity versus CO_2: $CH^{\delta+}\cdots F^{\delta+}$ interaction-driven binding sites for C_2H_2; weak CO_2-sorbent interactions.

Adsorption kinetics

Kinetics is a key factor in determining the efficiency of gas separations.[44] We, therefore, studied the pure gas adsorption kinetics for C_2H_2 and CO_2 for each of the activated samples (**SIFSIX-21-Ni**, **TIFSIX-4-Ni**, **NbOFFIVE-3-Ni**, **SIFSIX-21-Cu**, **TIFSIX-4-Cu**, and **NbOFFIVE-3-Cu**) by exposure to a constant flow of 10 cm^3min^{-1} of C_2H_2 or CO_2 at 303 K and 1.0 bar (Figures S54 and S55). After 5 cycles of C_2H_2 sorption, the order of uptakes were as follows: **SIFSIX-21-Cu** (7.8%) < **TIFSIX-4-Cu** (9.7%) < **NbOFFIVE-3-Cu** (10%) for the Cu(II) HUMs; **NbOFFIVE-3-Ni** (4.2%) ~ **TIFSIX-4-Ni** (4.3%) < **SIFSIX-21-Ni** (5.9%) for the Ni(II) HUMs (Figures S54 and S55). Meanwhile, the corresponding order after 3 cycles of CO_2 sorption were as follows: **NbOFFIVE-3-Cu** (0.73%) ~ **SIFSIX-21-Cu** (0.78%) < **TIFSIX-4-Cu** (1.5%) and **SIFSIX-21-Ni** (0.84%) ~ **TIFSIX-4-Ni** (0.85%) < **NbOFFIVE-3-Ni** (0.96%) for the Cu(II) and Ni(II) HUMs, respectively. The HUMs with the highest gravimetric uptakes, **NbOFFIVE-3-Cu** and **SIFSIX-21-Ni**, reached *ca.* 99% of their saturation uptakes in 54 and 35 min, respectively. For all HUMs, sorbent regeneration was conducted over five consecutive C_2H_2 adsorption/desorption cycles at 333 K under N_2 flow in <30 min (flow rate: 20 cm^3min^{-1}; Figures S54 andS55) for C_2H_2.

Dynamic column breakthrough (DCB) studies

Next, we investigated the C_2H_2/CO_2 separation performances of these HUMs through DCB experiments[57] with inlet gas mixture ratios 1:1 or 2:1 (v/v) for C_2H_2/CO_2.[1] Binary gas mixtures were passed through a fixed-bed reactor (8 mm diameter) filled with *ca.* 0.5 g of each HUM with a total gas flow rate of 1 cm^3min^{-1} at 1 bar and 298 K. Pre-activated samples were first heated at 333 K in a 20 cm^3min^{-1} flow of He to remove atmospheric impurities as monitored by gas chromatographic (GC) analysis of the effluent gas stream. The sorbent beds were then cooled to room temperature under continuous He flow and subjected to DCB experiments. Eluted gaseous components were continuously monitored through GC analysis (see supplemental information for details, Figure S56). Figure 3 reveals that CO_2 breakthrough occurred before that of C_2H_2 for each HUM and that **SIFSIX-21-Ni** was the best-performing sorbent, C_2H_2 breakthrough occurring at 363 and 298 min g^{-1} for the 1:1 and 2:1 gas mixtures, respectively. In contrast, the corresponding CO_2 breakthrough occurred at 152 and 114 min g^{-1} for the 1:1 and 2:1 gas mixtures, respectively. The time lags of 211 and 184 min g^{-1} between C_2H_2 and CO_2 breakthroughs for 1:1 and 2:1 gas mixtures, respectively, imply high C_2H_2 productivities.

GC data revealed that, for the 1:1 experiments, C_2H_2 levels in the effluent CO_2 gas stream were 623, 910, 1,751, 2,368, 2,368, and, 2,718 ppm for **SIFSIX-21-Ni**, **NbOFFIVE-3-Cu**, **TIFSIX-4-Cu**, **SIFSIX-21-Cu**, **TIFSIX-4-Ni**, and **NbOFFIVE-3-Ni**, respectively. Unlike the low uptakes of CO_2 registered in single-component isotherms (Figures 1D and 1E), 1:1 and 2:1 C_2H_2/CO_2 DCB experiments (Figure 3) revealed higher adsorbed CO_2 amounts indicated by coadsorption at lower partial pressures in dynamic experiments. Until C_2H_2 breakthrough occurred, CO_2 purity values in the effluent streams were found to be as follows: >99.9% for **SIFSIX-21-Ni** and

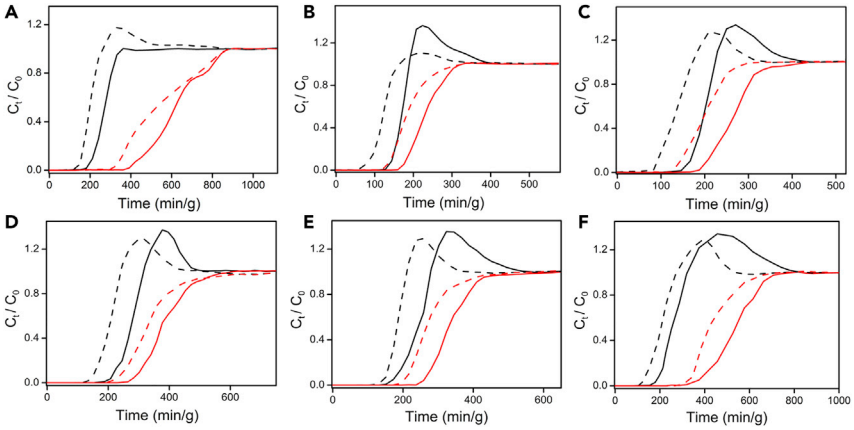

Figure 3. Experimental dynamic column breakthrough curves

(A–F) Binary C_2H_2/CO_2 mixture-based DCB experimental curves at 298 K and 1 bar on the studied family of pypz HUM sorbents (v/v = 1:1, solid line; 2:1, dashed line; C_2H_2, red; CO_2, black) (A), (B), and (C): **SIFSIX-21-Ni**, **TIFSIX-4-Ni**, and **NbOFFIVE-3-Ni**, respectively, and (D), (E), and (F): **SIFSIX-21-Cu**, **TIFSIX-4-Cu**, and **NbOFFIVE-3-Cu**, respectively (see details in the supplemental information).

NbOFFIVE-3-Cu; >99.7% for **TIFSIX-4-Cu**, **SIFSIX-21-Cu**, **TIFSIX-4-Ni**, and **NbOFFIVE-3-Ni**, i.e., higher than the commercial specification for CO_2 (N2.0, 99%). C_2H_2 uptakes calculated from the breakthrough curves for **SIFSIX-21-Ni**, **NbOFFIVE-3-Cu**, **TIFSIX-4-Cu**, **SIFSIX-21-Cu**, **TIFSIX-4-Ni**, and **NbOFFIVE-3-Ni** were observed to be 3.22, 3.08, 2.8, 3.07, 3.02, and 2.88 $mmol\,g^{-1}$, respectively (see supplemental information for details)[58,59]; these values are consistent with the respective isotherm-based uptakes at 0.5 bar. The DCB experiments enabled calculation of the separation selectivities (α_{AC}) for 1:1 and 2:1 C_2H_2:CO_2 mixtures: **SIFSIX-21-Ni** (27.7/10.0) > **NbOFFIVE-3-Cu** (16.9/7.9) > **NbOFFIVE-3-Ni** (15.0/6.5) > **TIFSIX-4-Cu** (5.4/4.1) > **SIFSIX-21-Cu** (4.6/3.1) > **TIFSIX-4-Ni** (4.4/3.1). **SIFSIX-21-Ni** exceeds the separation selectivities reported for **UTSA-74a** (20.1), **JXNU-5** (9.9), **JCM-1** (4.4), **FJU-89** (3), **SNNU-45** (2.9), **NKMOF-1-Ni** (2.6), **FJU-6-TATB** (2.3), **FJU-36a** (2.1), **HOF-3** (2), **SIFSIX-Cu-TPA** (1.97), **FJU-22a** (1.9), and **FeNi-M'MOF** (1.7) (Table S1). After full saturation in the equimolar DCB experiments, temperature programmed desorption measurements were conducted at 333 K (Figure S57). The desorption profiles revealed complete adsorbent regeneration in <120 min under a He flow of 20 $cm^3\,min^{-1}$ for **SIFSIX-21-Ni** and **NbOFFIVE-3-Cu**.

A mapping of α_{AC} versus equilibrium single-component C_2H_2 uptakes at 1 bar indicates that **SIFSIX-21-Ni**, **NbOFFIVE-3-Cu**, **NbOFFIVE-3-Ni**, **TIFSIX-4-Cu**, and **UTSA-74a** have potential to address the trade-off between adsorption capacity and separation selectivity for C_2H_2/CO_2 separation as they are the only sorbents that exhibit $\alpha_{AC} \geq 5$ and adsorption capacity $\geq 3.5\ mmol\,g^{-1}$ (see Figure 4A for a comparison of performance parameters). The UMCs in **UTSA-74a** require high temperature for activation (473 K under high vacuum (Figure 4A). Conversely, the HUM sorbents require heating to only 333 K for sorbent regeneration. Overall, **SIFSIX-21-Ni** outperforms the other HUMs reported herein like **UTSA-74a** and other known C_2H_2 selective sorbents thanks to its high separation selectivity (27.7), C_2H_2 uptake (4.0 $mmol\,g^{-1}$), and low regeneration temperature. Interestingly, the high C_2H_2/CO_2 separation selectivities for **M'FSIX-pypz-M**/**NbOFFIVE-pypz-M** can be attributed as much to weak CO_2 binding as to strong C_2H_2 affinity as reflected in $(\Delta Q_{st})_{AC}$ values. **SIFSIX-21-Ni** exhibits a relatively low $Q_{st}(CO_2)$ of 19.8 $kJ\,mol^{-1}$ at low loading versus other C_2H_2 selective physisorbents

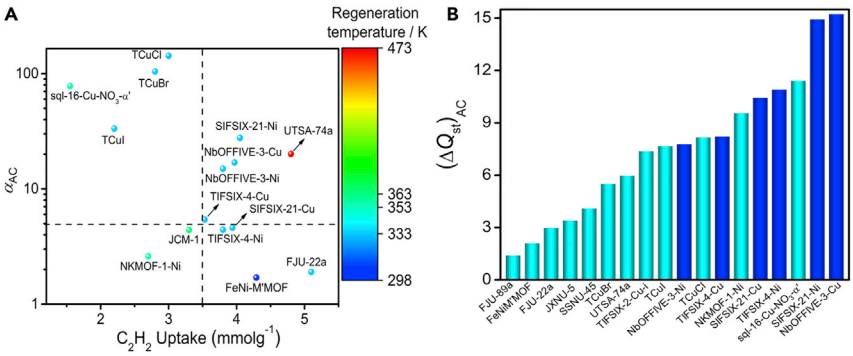

Figure 4. Comparison of separation selectivity versus uptake capacity and ΔQ_{st}

(A) Comparison of C_2H_2/CO_2 separation selectivity α_{AC} (v/v = 1:1) and gravimetric C_2H_2 uptake at 1 bar in benchmark C_2H_2/CO_2 separating adsorbents; regeneration/activation temperatures (range 298 to 473 K shown on the right side).

(B) Comparison of $(\Delta Q_{st})_{AC}$ for the best-performing adsorbents at half loadings.

(Table S1), resulting in a high $(\Delta Q_{st})_{AC}$ of 18.1 kJ mol^{-1}. Indeed, $(\Delta Q_{st})_{AC}$ at low loading for **SIFSIX-21-Ni** is close to that of **NKMOF-1-Ni** (19.4) kJ mol^{-1} (Figure S59), which exhibits an exceptionally high $Q_{st}(C_2H_2)$ of 60.3 kJ mol^{-1}. However, as Figure S58 reveals, the $Q_{st}(C_2H_2)$ for **NKMOF-1-Ni** rapidly declines to 46.0 kJ mol^{-1} at half loading, at which point $(\Delta Q_{st})_{AC}$ is reduced to 9.5 kJ mol^{-1} (Figure 4B). $(\Delta Q_{st})_{AC}$ values at zero coverage, although widely used, tend to overestimate separation performance at relevant partial pressures. In our experience, for most C_2H_2 selective sorbents, particularly those with high surface areas, $Q_{st}(C_2H_2)$ at half and full coverage decline from their zero loading values because of weak multilayer adsorption. Therefore, comparing $(\Delta Q_{st})_{AC}$ at low coverage does not always translate well to a prediction of relative binding affinity and is why we consider $(\Delta Q_{st})_{AC}$ at half loading to be a suitable metric to estimate relative binding for an equimolar mixture.[42] Figure 4B reveals that **NbOFFIVE-3-Cu** and **SIFSIX-21-Ni** set new benchmarks of $(\Delta Q_{st})_{AC}$ values at half loading, 15.2 and 14.9 kJmol^{-1}, respectively. This result is consistent with their DCB separation performances especially higher α_{AC} relative to those of **TIFSIX-4-Ni**, **SIFSIX-21-Cu**, **TIFSIX-4-Cu**, and **NbOFFIVE-3-Ni**. Overall, $(\Delta Q_{st})_{AC}$ values of at least 7.5 kJmol^{-1} for all HUMs reported herein suggests thermodynamic preference for C_2H_2 over CO_2 and correlates well with their high α_{AC} values.

Spectroscopic studies

In situ *infrared spectroscopy*

To further probe the binding sites of C_2H_2 and CO_2 in these HUMs, we carried out *in situ* infrared (IR) spectroscopy measurements of C_2H_2 and CO_2 adsorption in the two best-performing adsorbents, **NbOFFIVE-3-Cu** and **SIFSIX-21-Ni**. The difference spectra for **NbOFFIVE-3-Cu** (Figure 5) and **SIFSIX-21-Ni** (Figure S60) demonstrate characteristic stretching bands for adsorbed C_2H_2 and CO_2 molecules, i.e., $\nu_{as}(C_2H_2)$ at 3,309–3,209 cm^{-1} and $\nu_{as}(CO_2)$ at 2,338 cm^{-1}, whereas the perturbations of vibrational bands in the HUMs are characterized by the decrease in $\nu(CH)_{phenyl}$ peak intensity and its derivative feature in the shorter region, 1,700–1,000 cm^{-1}. The perturbed bands $\nu(CH)_{phenyl}$, $\nu(CC)_{phenyl}$, $\delta(CH)_{ip,\ phenyl}$, and $\nu(CN)_{phenyl}$ (see Figures 5, S60, and S61) indicate that C_2H_2 and CO_2 interact with the linker ligand's phenyl rings,[60] as predicted computationally (Figure 2). Analysis of these data revealed that concomitant loading of C_2H_2 perturbs the vibrational bands of the HUMs more than CO_2, which is also indicative of stronger sorbent-sorbate interactions for C_2H_2. Particularly, two distinct $\nu_{as}(C_2H_2)$ bands are present at 3,209 and 3,309 cm^{-1} in both **NbOFFIVE-3-Cu** and **SIFSIX-21-Ni**. These bands suggest two types of C_2H_2 binding

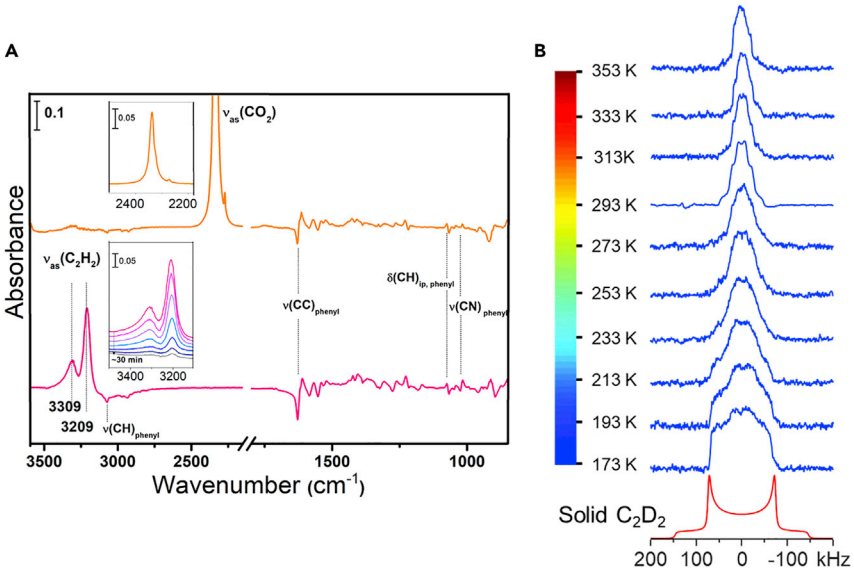

Figure 5. *In situ* infrared spectra and ^{2}H static NMR spectra

(A) Difference IR spectra showing the adsorbed CO_2 (orange) and C_2H_2 (pink) upon loading at 298 K and 1 bar adsorbate pressure into **NbOFFIVE-3-Cu** and subsequent evacuation of the gas phase within 3 s, respectively. Each is referenced to the spectrum of activated HUMs. Top inset shows the $\nu_{as}(CO_2)$ band and the bottom inset shows the decay of $\nu_{as}(C_2H_2)$ bands under vacuum. Notation and acronym: ν, stretching; δ, deformation; *ip*, in plane.

(B) Experimental ^{2}H static NMR spectra of C_2D_2 adsorbed in **NbOFFIVE-3-Cu** (at a loading level of 0.4 C_2D_2 per Cu) as a function of temperature (blue lines) and simulated ^{2}H spectrum of static C_2D_2 (red line).

sites with different binding strengths. This is in contrast to adsorbed CO_2, which displays a single peak at 2,338 cm^{-1} in the corresponding IR spectrum, indicating only a single type of adsorbed CO_2 molecule. The 3,209 cm^{-1} IR band decays slightly slower than the one at 3,309 cm^{-1} (Figure S63), also implying stronger C_2H_2 binding inside the HUMs. Higher relative intensity suggests that the stronger binding sites are more populated with C_2H_2. C_2H_2 is well-known to be relatively acidic (pK_a = 25) in the context of hydrocarbons and, thus, tends to form hydrogen bonding interactions, as observed in several MOMs.[56,61] Similar to the well-studied OH or N-H stretch vibrations,[62] the $\nu_{as}(C_2H_2)$ band undergoes a downward shift with respect to the gas phase value (at 3,287 cm^{-1}) upon forming intermolecular hydrogen bonds. The 3,209 cm^{-1} band represents a red-shift of 78 cm^{-1} and is consistent with the C_2H_2 binding site identified by simulation in Figure 2A. Overall, these *in situ* IR studies support the high adsorption selectivities for C_2H_2 over CO_2.

SOLID-STATE NMR SPECTROSCOPY

Solid-state NMR spectroscopy is a powerful technique for investigating the behavior of gaseous molecules adsorbed by porous materials.[63–65] To better understand the adsorptive properties of the HUMs studied herein, ^{13}C and ^{2}H static solid-state NMR experiments were conducted to directly monitor the behavior of $^{13}CO_2$ and C_2D_2 molecules adsorbed by **NbOFFIVE-3-Cu**. Figure S64 illustrates the ^{13}C NMR spectra of **NbOFFIVE-3-Cu** loaded with ^{13}C-labeled CO_2 at various temperatures. At 373 K, the spectrum contains a relatively sharp, symmetric peak at 125 ppm superimposed on a very broad profile. Comparing the spectrum of the HUM loaded with CO_2 with the spectrum of the empty HUM (Figure S64) indicates that the broad resonance in the spectrum of CO_2-loaded HUM likely originates from the linkers in the framework.

The position of the sharp signal indicates that this signal is from adsorbed CO_2. The sharpness of the resonance suggests that CO_2 molecules are rather mobile, implying weak interaction of CO_2 with the framework. Considering that ^{13}C enrichment of $^{13}CO_2$ is 99% and that the framework carbon atoms are at natural abundance (1.1%), the relative intensity of the two signals suggests that a relatively small amount of CO_2 was adsorbed by the HUM, which is consistent with the poor S/N ratio of the spectrum. Previous studies showed that for MOMs featuring good affinity toward CO_2, the ^{13}C spectra of adsorbed CO_2 usually exhibited a significantly higher intensity under similar adsorption conditions.[66–68] Overall, the ^{13}C NMR results indicate that **NbOFFIVE-3-Cu** does not adsorb CO_2 well. It is worth noting that the isotropic chemical shift of adsorbed CO_2 (125 ppm) is the same as that of CO_2 adsorbed in the diamagnetic MOMs,[66–68] suggesting the lack of a significant paramagnetic interaction between CO_2 and Cu(II). This is likely due to the distances between the carbon of CO_2 and nearby paramagnetic metal ions being rather long, i.e., 8.03, 7.16, 6.03, 6.31 Å (Figure S65), and that CO_2 is highly mobile. Similar situations have been observed in other Cu(II)-MOMs.[69,70] Upon lowering the temperature, the sharp characteristic peak of CO_2 gradually became broader and merged with the broad framework peak at 253 K. We attribute this to reduced mobility of CO_2 with decreasing temperature and chemical shift anisotropy, which is largely averaged by molecular motions at higher temperatures, becoming dominant and broadening the signal.

In contrast to the ^{13}C spectra of CO_2 loaded in **NbOFFIVE-3-Cu**, the ^{2}H static NMR spectra of C_2D_2 loaded in this HUM exhibited much stronger signals (Figure 5B), suggesting that **NbOFFIVE-3-Cu** has a higher affinity for C_2D_2 versus CO_2 under the same loading conditions. The ^{2}H static spectrum of adsorbed C_2D_2 at room temperature (293 K) exhibits a narrow pattern, suggesting a lack of significant paramagnetic interaction between the deuterons of C_2D_2 and Cu(II). This is consistent with the modeling study herein that indicates that two deuterium atoms in C_2D_2 are distant from nearby metal centers (5.1–6.4 Å). Inspection of the spectrum also reveals a well-defined line-shape with characteristic horns, shoulders, and "feet." However, such a pattern cannot be simulated by a single site. Instead, analytical simulation using WSolids software[71] revealed two components: a narrower component with a quadrupolar coupling constant (C_Q) of 43 kHz and a non-zero asymmetry parameter (η_Q) of 0.60 and a broader component with a C_Q of 65 kHz and η_Q of 0.0 (Figure S66B). The overall breadths of both patterns are markedly smaller than that of a static C_2D_2 (Figure 5B), which has a C_Q of 198 kHz and $\eta_Q = 0$.[72] This observation indicates that the first-order quadrupolar interaction is averaged by molecular motions experienced by C_2D_2. Seeing two separate patterns suggests that there are two types of C_2D_2 molecules in the unit cell and that they undergo different motions. In an attempt to identify the types of motions, dynamic simulations were performed by using the Express software package.[73] Based on the simulation results, we propose that the narrower pattern results from the C_2D_2 molecules that simultaneously undergo two motions: (1) localized wobbling motion modeled by a C_3 rotation and (2) a delocalized hopping about a C_2 axis (Figure S66D). A small portion (around 10%) of C_2D_2 only wobbles at its absorption site (Figure S66C), yielding a broader line. The spectra between 293 and 353 K look similar, implying that the motions are in the fast exchange regime. In the temperature range 273–173 K, the pattern for each spectrum is gradually broadened and loses its characteristic discontinuities. The overall breadth of the pattern at 173 K is much broader than at 293 K, inferring that C_2D_2 adsorbed by the HUM becomes much less mobile. However, it is difficult to analyze the spectra at low temperature. When loading was increased, the ^{2}H spectrum comprised a sharp peak in the middle and a broad component at the bottom (Figure S67). The sharp peak is likely due to the C_2D_2 molecules inside the pores undergoing fast exchange with the C_2D_2 outside the HUM. They

do not interact with the framework strongly. The broad component is attributed to C_2D_2 molecules inside the pores that have strong interactions with the framework. The preference of C_2H_2 versus CO_2 indicated by solid-state NMR spectra further supports our results from single-component sorption, DCB experiments, molecular modeling, and *in situ* FTIR spectroscopic studies.

Accelerated stability tests[74] (313 K and 75% RH for 14 days) revealed that **NbOFFIVE-3-Ni**, **SIFSIX-21-Cu**, **TIFSIX-4-Cu**, and **NbOFFIVE-3-Cu** exhibit excellent hydrolytic stability (Figures S68C–S68F). Accelerated stability tests also revealed that both **SIFSIX-21-Ni** and **TIFSIX-4-Ni** (Figures S68A and S68B) underwent a phase change after exposure to humidity. Such phase changes have been observed in other HUMs and were attributed to inorganic pillar ligands being replaced by aqua ligands to afford corresponding **sql** networks.[75] **SIFSIX-21-Ni** was regenerated by heating the humidity-exposed sample at 358 K for 10 h in MeOH (Figure S69), whereas **TIFSIX-4-Ni** was regenerated by heating at 393 K (Figure S70).

Conclusions

In summary, six new HUMs, **SIFSIX-21-Ni**, **TIFSIX-4-Ni**, **NbOFFIVE-3-Ni**, **SIFSIX-21-Cu**, **TIFSIX-4-Cu**, and **NbOFFIVE-3-Cu**, were studied with respect to their ability to separate C_2H_2 from CO_2. Single-component sorption isotherms and equimolar C_2H_2/CO_2 binary gas mixture DCB experiments revealed that four of these HUMs, **SIFSIX-21-Ni**, **NbOFFIVE-3-Ni**, **TIFSIX-4-Cu**, and **NbOFFIVE-3-Cu**, break the trade-off between high adsorption capacities ≥ 3.5 mmol·g^{-1} and high separation selectivities ≥ 5. **SIFSIX-21-Ni** outperformed all sorbents thanks to its benchmark separation selectivity (27.7) and high adsorption capacity (4 mmol·g^{-1}). The key to the performance of **SIFSIX-21-Ni** is pore size and chemistry that enables relatively high surface area and strong C_2H_2 binding sites. This study once again highlights the ability of ultramicroporous sorbents to offer hitherto unattainable selectivity values for key binary gas separations.[25]

EXPERIMENTAL PROCEDURES

Resource availability

Lead contact

Further information and requests for resources should be directed to and will be fulfilled by the lead contact, Michael J. Zaworotko (xtal@ul.ie).

Materials availability

All materials generated in this study are available from the lead contact on request.

Data and code availability

The accession number for the crystal structures reported in this paper is Cambridge Crystallographic Data Centre, CCDC: 2052024, 2052025, 2052046, and 2052047.

SUPPLEMENTAL INFORMATION

Supplemental information can be found online at https://doi.org/10.1016/j.chempr.2021.07.007.

ACKNOWLEDGMENTS

M.J.Z. acknowledges the support of the Science Foundation Ireland (SFI awards 13/RP/B2549 and 16/IA/4624) and the European Research Council (award ADG 885695). T.P., K.A.F., and B.S. acknowledge the National Science Foundation (award no. DMR-1607989), including support from the Major Research

Instrumentation Program (award no. CHE-1531590). P.E.K gratefully acknowledges the MacDiarmid Institute for Advanced Materials and Nanotechnology. Computational resources were made available by an XSEDE grant (no. TG-DMR090028) awarded to B.S. and by Research Computing at the University of South Florida. We thank Matthew Mostrom for his assistance with calculating the partial charges. K.T. acknowledges the U. S. Department of Energy, Office of Science, Basic Energy Sciences under award no. DE-SC0019902. Y.H. thanks the Natural Science and Engineering Research Council (NSERC) of Canada for a Discovery Grant. M.V. acknowledges the Irish Centre for High-End Computing (ICHEC) for the provision of computational facilities and support.

AUTHOR CONTRIBUTIONS

Conceptualization, N.K., S.M., and M.J.Z.; methodology, N.K. and S.M.; validation, N.K., S.M., N.C.H.-R., and A.A.B.; investigation, N.K., S.M., N.C.H.-R., A.A.B., K.T., V.M., L.M.v.W., K.O., and K.M.P.; formal analysis, M.V., T.P., and K.A.F.; resources, N.H.R. and A.K.; data curation, N.K., S.M., A.A.B., M.V., T.P., and K.A.F.; writing – original draft, N.K., S.M., N.H.R., A.A.B., K.T., V.M., M.V., T.P., Y.H., and M.J.Z; writing – review & editing, all authors; funding acquisition, K.T., L.B., B.S., Y.H., P.E.K., and M.J.Z; supervision, M.J.Z.

DECLARATION OF INTERESTS

The authors declare no competing interests.

Received: January 10, 2021
Revised: February 25, 2021
Accepted: July 13, 2021
Published: August 10, 2021

REFERENCES

1. Pässler, P., Hefner, W., Buckl, K., Meinass, H., Meiswinkel, A., Wernicke, H.-J., Ebersberg, G., Müller, R., Bässler, J., Behringer, H., et al. (2011). Acetylene. In Ullmann's Encyclopedia of Industrial Chemistry (Wiley).

2. Himbert, G. (1996). Book review: modern acetylene chemistry. In Angew. Chem. Int. Ed. Engl., *35*, P.J. Stang and F. Diederich, eds., pp. 2154–2155.

3. Lower and upper explosive limits for flammable gases and vapors(LEL/UEL). https://www.chrysalisscientific.com/pg443-Lower-LEL-Upper-UEL-Explosive-Limits.pdf.

4. Gannon, R.E., Krukonis, V.J., and Schoenberg, T. (1970). Conversion of coal to acetylene in arc-heated hydrogen. Prod. R D *9*, 343–347.

5. Granada, A., Karra, S.B., and Senkan, S.M. (1987). Conversion of methane into acetylene and ethylene by the chlorine-catalyzed oxidative-pyrolysis (CCOP) process. 1. Oxidative pyrolysis of chloromethane. Ind. Eng. Chem. Res. *26*, 1901–1905.

6. Guo, C.J., Shen, D., and Bülow, M. (2001). 18-O-03 - Kinetic separation of binary mixtures of carbon dioxide and C2 hydrocarbons on modified LTA-type zeolites. Studies in Surface Science and Catalysis *135*, 144.

7. Arpe, H.-J., and Weissermel, K. (2003). Aromatics — production and conversion. In Industrial Organic Chemistry, Fourth Edition Edition (Wiley-VCH Press), pp. 313–336.

8. Thanh, C.N., Didillon, B., Sarrazin, P., and Cameron, S. (1996). Selective hydrogenation catalyst and a process using that catalyst. US patent US6054409A, filed December 20, 1996, and granted April 25, 2000.

9. Xu, G.L.F., Yang, Y., Hu, Y., Zhang, K., and Liu, W. (2014). An improved CO_2 separation and purification system based on cryogenic separation and distillation. Energies *7*, 3484–3502.

10. Nugent, P., Belmabkhout, Y., Burd, S.D., Cairns, A.J., Luebke, R., Forrest, K., et al. (2013). Porous materials with optimal adsorption thermodynamics and kinetics for CO_2 separation. Nature *495*, 80–84.

11. Mukherjee, S., Sikdar, N., O'Nolan, D., Franz, D.M., Gascón, V., Kumar, A., et al. (2019). Trace CO_2 capture by an ultramicroporous physisorbent with low water affinity. Sci. Adv. *5*, eaax9171.

12. Couck, S., Denayer, J.F.M., Baron, G.V., Rémy, T., Gascon, J., and Kapteijn, F. (2009). An amine-functionalized MIL-53 metal−organic framework with large separation power for CO_2 and CH_4. J. Am. Chem. Soc. *131*, 6326–6327.

13. Cui, X., Chen, K., Xing, H., Yang, Q., Krishna, R., Bao, Z., Wu, H., Zhou, W., Dong, X., Han, Y., et al. (2016). Pore chemistry and size control in hybrid porous materials for acetylene capture from ethylene. Science *353*, 141–144.

14. Li, B., Cui, X., O'Nolan, D., Wen, H.-M., Jiang, M., Krishna, R., Wu, H., Lin, R.-B., Chen, Y.-S., Yuan, D., et al. (2017). An ideal molecular sieve for acetylene removal from ethylene with record selectivity and productivity. Adv. Mater. *29*, 1704210.

15. Chen, C., Wei, Z., Pham, T., Lan, P.C., Zhang, L., Forrest, K.A., Chen, S., Al-Enizi, A.M., Nafady, A., Su, C., et al. (2021). Nanospace engineering of metal–organic frameworks through dynamic spacer installation of multifunctionalities for efficient separation of ethane from ethane/ethylene mixtures. Angew. Chem. Int. Ed. *60*, 9680–9685.

16. Lin, R.-B., Xiang, S., Zhou, W., and Chen, B. (2020). Microporous metal-organic framework materials for gas separation. Chem *6*, 337–363.

17. Matsuda, R., Kitaura, R., Kitagawa, S., Kubota, Y., Belosludov, R.V., Kobayashi, T.C., Sakamoto, H., Chiba, T., Takata, M., Kawazoe, Y., and Mita, Y. (2005). Highly controlled acetylene accommodation in a metal–organic microporous material. Nature *436*, 238–241.

18. Li, J.R., Kuppler, R.J., and Zhou, H.C. (2009). Selective gas adsorption and separation in

metal–organic frameworks. Chem. Soc. Rev. *38*, 1477–1504.

19. Sircar, S. (2006). Basic Research needs for design of adsorptive gas separation processes. Ind. Eng. Chem. Res. *45*, 5435–5448.

20. Cui, W.G., Hu, T.L., and Bu, X.H. (2020). Metal–organic framework materials for the separation and purification of light hydrocarbons. Adv. Mater. *32*, e1806445.

21. Perry, J.J., Perman, J.A., and Zaworotko, M.J. (2009). Design and synthesis of metal–organic frameworks using metal–organic polyhedra as supermolecular building blocks. Chem. Soc. Rev. *38*, 1400–1417.

22. MacGillivray, R. (2010). Metal-Organic Frameworks: Design and Application (John Wiley & Sons).

23. Schröder, M., and Banerjee, M. (2009). Functional Metal-Organic Frameworks: Gas Storage, Separation and Catalysis (Springer-Verlag).

24. Kitagawa, S., Kitaura, R., and Noro, S.-i. (2004). Functional porous coordination polymers. Angew. Chem. Int. Ed. Engl. *43*, 2334–2375.

25. Mukherjee, S., Sensharma, D., Chen, K.J., and Zaworotko, M.J. (2020). Crystal engineering of porous coordination networks to enable separation of C2 hydrocarbons. Chem. Commun. (Camb) *56*, 10419–10441.

26. CCDC (2020). New data and improvements - 2020.3 CSD data release. https://www.ccdc.cam.ac.uk/Community/blog/New_Data_and_improvements_2020.3_blog/.

27. Niu, Z., Cui, X., Pham, T., Verma, G., Lan, P.C., Shan, C., et al. (2021). A MOF-based ultra-strong acetylene nano-trap for highly efficient C_2H_2/CO_2 separation. Angew. Chem. Int. Ed. Engl. *60*, 5283–5288.

28. Di, Z., Liu, C., Pang, J., Chen, C., Hu, F., Yuan, D., et al. (2021). Cage-like porous materials with simultaneous high C_2H_2 storage and excellent C_2H_2/CO_2 separation performance. Angew. Chem. Int. Ed. Engl. *60*, 10828–10832.

29. Li, H., Liu, C., Chen, C., Di, Z., Yuan, D., Pang, J., Wei, W., Wu, M., and Hong, M. (2021). An unprecedented pillar–cage fluorinated hybrid porous framework with highly efficient acetylene storage and separation. Angew. Chem. Int. Ed. Engl. *60*, 7547–7552.

30. Mukherjee, S., He, Y., Franz, D., Wang, S.Q., Xian, W.R., Bezrukov, A.A., et al. (2020). Halogen–C_2H_2 binding in ultramicroporous metal–organic frameworks (MOFs) for benchmark C_2H_2/CO_2 separation selectivity. Chem. Eur. J. *26*, 4923–4929.

31. Lee, J., Chuah, C.Y., Kim, J., Kim, Y., Ko, N., Seo, Y., Kim, K., Bae, T.H., and Lee, E. (2018). Separation of acetylene from carbon dioxide and ethylene by a water-stable microporous metal–organic framework with aligned imidazolium groups inside the channels. Angew. Chem. Int. Ed. Engl. *57*, 7869–7873.

32. Peng, Y.L., Pham, T., Li, P., Wang, T., Chen, Y., Chen, K.J., Forrest, K.A., Space, B., Cheng, P., Zaworotko, M.J., and Zhang, Z. (2018). Robust ultramicroporous metal–organic frameworks with benchmark affinity for acetylene. Angew. Chem. Int. Ed. Engl. *57*, 10971–10975.

33. Yao, Z., Zhang, Z., Liu, L., Li, Z., Zhou, W., Zhao, Y., et al. (2016). Extraordinary separation of acetylene-containing mixtures with microporous metal–organic frameworks with open O donor sites and tunable robustness through control of the helical chain secondary building units. Chem. Eur. J. *22*, 5676–5683.

34. Ye, Y., Chen, S., Chen, L., Huang, J., Ma, Z., Li, Z., Yao, Z., Zhang, J., Zhang, Z., and Xiang, S. (2018). Additive-induced supramolecular isomerism and enhancement of robustness in Co(II)-based MOFs for efficiently trapping acetylene from acetylene-containing mixtures. ACS Appl. Mater. Interfaces *10*, 30912–30918.

35. Li, P., He, Y., Zhao, Y., Weng, L., Wang, H., Krishna, R., et al. (2015). A rod-packing microporous hydrogen-bonded organic framework for highly selective separation of C_2H_2/CO_2 at room temperature. Angew. Chem. Int. Ed. Engl. *54*, 574–577.

36. Liu, L., Yao, Z., Ye, Y., Yang, Y., Lin, Q., Zhang, Z., et al. (2020). Integrating the pillared-layer strategy and pore-space partition method to construct multicomponent MOFs for C_2H_2/CO_2 separation. J. Am. Chem. Soc. *142*, 9258–9266.

37. Li, Y.P., Wang, Y., Xue, Y.Y., Li, H.P., Zhai, Q.G., Li, S.N., Jiang, Y.C., Hu, M.C., and Bu, X. (2019). Ultramicroporous building units as a path to bi-microporous metal–organic frameworks with high acetylene storage and separation performance. Angew. Chem. Int. Ed. Engl. *58*, 13590–13595.

38. Liu, R., Liu, Q.Y., Krishna, R., Wang, W., He, C.T., and Wang, Y.L. (2019). Water-stable europium 1,3,6,8-Tetrakis(4-carboxylphenyl) pyrene framework for efficient C_2H_2/CO_2 separation. Inorg. Chem. *58*, 5089–5095.

39. Liu, L., Yao, Z., Ye, Y., Chen, L., Lin, Q., Yang, Y., Zhang, Z., and Xiang, S. (2018). Robustness, selective gas separation, and nitrobenzene sensing on two isomers of cadmium metal–organic frameworks containing various metal–O–metal chains. Inorg. Chem. *57*, 12961–12968.

40. Gao, J., Qian, X., Lin, R.-B., Krishna, R., Wu, H., Zhou, W., et al. (2020). Mixed metal–organic framework with multiple binding sites for efficient C_2H_2/CO_2 separation. Angew. Chem. Int. Ed. *59*, 4396–4400.

41. Luo, F., Yan, C., Dang, L., Krishna, R., Zhou, W., Wu, H., Dong, X., Han, Y., Hu, T.L., O'Keeffe, M., et al. (2016). UTSA-74: a MOF-74 isomer with two accessible binding sites per metal center for zhighly selective gas separation. J. Am. Chem. Soc. *138*, 5678–5684.

42. Kumar, N., Mukherjee, S., Bezrukov, A.A., Vandichel, M., Shivanna, M., Sensharma, D., et al. (2020). A square lattice topology coordination network that exhibits highly selective C_2H_2/CO_2 separation performance. SmartMat *1*, e1008.

43. Mukherjee, S., Kumar, A., and Zaworotko, M.J. (2019). 2 - Metal-organic framework based carbon capture and purification technologies for clean environment. In Metal-Organic Frameworks (MOFs) for Environmental Applications, S.K. Ghosh, ed. (Elsevier), pp. 5–61.

44. Oschatz, M., and Antonietti, M. (2018). A search for selectivity to enable CO_2 capture with porous adsorbents. Energy Environ. Sci. *11*, 57–70.

45. Scott, H.S., Bajpai, A., Chen, K.-J., Pham, T., Space, B., Perry, J.J., et al. (2015). Novel mode of 2-fold interpenetration observed in a primitive cubic network of formula [Ni(1,2-bis(4-pyridyl)acetylene)$_2$(Cr_2O_7)]n. Chem. Commun. *51*, 14832–14835.

46. Bhatt, P.M., Belmabkhout, Y., Cadiau, A., Adil, K., Shekhah, O., Shkurenko, A., et al. (2016). A fine-tuned fluorinated MOF addresses the needs for trace CO_2 removal and air capture using physisorption. J. Am. Chem. Soc. *138*, 9301–9307.

47. Mukherjee, S., and Zaworotko, M.J. (2020). Crystal engineering of hybrid coordination networks: From form to function. Trends in Chemistry *2*, 506–518.

48. Howarth, A.J., Peters, A.W., Vermeulen, N.A., Wang, T.C., Hupp, J.T., and Farha, O.K. (2017). Best practices for the synthesis, activation, and characterization of metal–organic frameworks. Chem. Mater. *29*, 26–39.

49. Myers, A.L., and Prausnitz, J.M. (1965). Thermodynamics of mixed-gas adsorption. AIChE J *11*, 121–127.

50. Qazvini, O.T., Babarao, R., and Telfer, S.G. (2019). Multipurpose metal–organic framework for the adsorption of acetylene: ethylene purification and carbon dioxide removal. Chem. Mater. *31*, 4919–4926.

51. Duan, X., Zhang, Q., Cai, J., Yang, Y., Cui, Y., He, Y., Wu, C., Krishna, R., Chen, B., and Qian, G. (2014). A new metal–organic framework with potential for adsorptive separation of methane from carbon dioxide, acetylene, ethylene, and ethane established by simulated breakthrough experiments. J. Mater. Chem. A *2*, 2628–2633.

52. Wen, H.M., Liao, C., Li, L., Yang, L., Wang, J., Huang, L., et al. (2019). Reversing C_2H_2–CO_2 adsorption selectivity in an ultramicroporous metal–organic framework platform. Chem. Commun. (Camb) *55*, 11354–11357.

53. Chen, K.-J., Scott, H.S., Madden, D.G., Pham, T., Kumar, A., Bajpai, A., et al. (2016). Benchmark C_2H_2/CO_2 and CO_2/C_2H_2 separation by two closely related hybrid ultramicroporous materials. Chem *1*, 753–765.

54. Yoon, J.W., Lee, J.S., Lee, S., Cho, K.H., Hwang, Y.K., Daturi, M., et al. (2015). Adsorptive separation of acetylene from light hydrocarbons by mesoporous iron Trimesate MIL-100(Fe). Chem. Eur. J. *21*, 18431–18438.

55. Wellendorff, J., Lundgaard, K.T., Møgelhøj, A., Petzold, V., Landis, D.D., Nørskov, J.K., Bligaard, T., and Jacobsen, K.W. (2012). Density functionals for surface science: exchange-correlation model development with Bayesian error estimation. Phys. Rev. B *85*, 235149.

56. Chen, K.J., Madden, D.G., Mukherjee, S., Pham, T., Forrest, K.A., Kumar, A., Space, B., Kong, J., Zhang, Q.Y., and Zaworotko, M.J. (2019). Synergistic sorbent separation for one-step ethylene purification from a four-component mixture. Science *366*, 241–246.

57. Rajendran, A., Kariwala, V., and Farooq, S. (2008). Correction procedures for extra-column effects in dynamic column breakthrough experiments. Chem. Eng. Sci. *63*, 2696–2706.

58. Shen, J., He, X., Ke, T., Krishna, R., van Baten, J.M.V., Chen, R., Bao, Z., Xing, H., Dincă, M., Zhang, Z., et al. (2020). Simultaneous interlayer and intralayer space control in two-dimensional metal−organic frameworks for acetylene/ethylene separation. Nat. Commun. *11*, 6259.

59. Zhang, Z., Tan, B., Wang, P., Cui, X., and Xing, H. (2020). Highly efficient separation of linear and branched C4 isomers with a tailor-made metal–organic framework. AIChE J *66*, e16236.

60. Swoboda, A.R., and Kunze, G.W. (1964). Infrared study of pyridine adsorbed on montmorillonite surfaces. Clays Clay Miner *13*, 277–288.

61. Nijem, N., Wu, H.H., Canepa, P., Marti, A., Balkus, K.J., Thonhauser, T., Li, J., and Chabal, Y.J. (2012). Tuning the gate opening pressure of metal-organic frameworks (MOFs) for the selective separation of hydrocarbons. J. Am. Chem. Soc. *134*, 15201–15204.

62. Marechal, Y. (2007). The Hydrogen Bond and the Water Molecule: the Physics and Chemistry of Water, Aqueous and Bio-Media (Elsevier Science).

63. Wong, Y.T.A., Martins, V., Lucier, B.E.G., and Huang, Y. (2019). Solid-state NMR spectroscopy: a powerful technique to directly study small gas molecules adsorbed in metal-organic frameworks. Chem. Eur. J. *25*, 1848–1853.

64. Bertmer, M. (2020). Solid-state NMR of small molecule adsorption in metal–organic frameworks (MOFs). Annu. Rep. NMR Spectrosc. *101*, 1–64.

65. Witherspoon, V.J., Xu, J., and Reimer, J.A. (2018). Solid-state NMR investigations of carbon dioxide gas in metal–organic frameworks: insights into molecular motion and adsorptive behavior. Chem. Rev. *118*, 10033–10048.

66. Zhang, Y., Lucier, B.E.G., and Huang, Y. (2016). Deducing CO_2 motion, adsorption locations and binding strengths in a flexible metal–organic framework without open metal sites. Phys. Chem. Chem. Phys. *18*, 8327–8341.

67. Lu, Y., Lucier, B.E.G., Zhang, Y., Ren, P., Zheng, A., and Huang, Y. (2017). Sizable dynamics in small pores: CO_2 location and motion in the α-Mg formate metal–organic framework. Phys. Chem. Chem. Phys. *19*, 6130–6141.

68. Wu, B., Wong, Y.T.A., Lucier, B.E.G., Boyle, P.D., and Huang, Y. (2019). Exploring host-guest interactions in the α-$Zn_3(HCOO)_6$ metal-organic framework. ACS Omega *4*, 4000–4011.

69. Chen, M., Chen, S., Chen, W., Lucier, B.E.G., Zhang, Y., Zheng, A., and Huang, Y. (2018). Analyzing gas adsorption in an amide-functionalized metal organic framework: are the carbonyl or amine groups responsible? Chem. Mater. *30*, 3613–3617.

70. Gul-E-Noor, F., Mendt, M., Michel, D., Pöppl, A., Krautscheid, H., Haase, J., et al. (2013). Adsorption of Small Molecules on $Cu_3(btc)_2$ and $Cu_{3-x}Zn_x(btc)_2$ Metal–Organic Frameworks (MOF) As Studied by Solid-State NMR. J. Phys. Chem. C *117*, 7703–7712.

71. Eichele, K. (2011). WSolids1, Version 1.20.15 (Tübingen, Germany: Universität Tübingen). http://anorganik.uni-tuebingen.de/klaus/soft/wsolids1/wsolids1.pdf.

72. Millett, F.S., and Dailey, B.P. (1972). NMR determination of some deuterium quadrupole coupling constants in nematic solutions. J. Chem. Phys. *56*, 3249–3256.

73. Vold, R.L., and Hoatson, G.L. (2009). Effects of jump dynamics on solid state nuclear magnetic resonance line shapes and spin relaxation times. J. Magn. Reson. *198*, 57–72.

74. Waterman, K.C. (2009). Understanding and predicting pharmaceutical product shelf-life. In Handbook of Stability Testing in Pharmaceutical Development: Regulations, Methodologies, and Best Practices, K. Huynh-Ba, ed. (Springer), pp. 115–135.

75. O'Nolan, D., Kumar, A., and Zaworotko, M.J. (2017). Water vapor sorption in hybrid pillared square grid materials. J. Am. Chem. Soc. *139*, 8508–8513.